

## A Catalog of 486 Barium Stars Identified in GALAH DR4

Guochao Yang,<sup>1,2,\*</sup> Jingkun Zhao,<sup>2,†</sup> Nian Liu,<sup>1,‡</sup> Xiaokun Hou,<sup>2</sup> Zhenxin Lei,<sup>3</sup> Xianhao Ye,<sup>2,4,5</sup> and Gang Zhao<sup>2,6</sup>

<sup>1</sup>School of Physics and Astronomy, China West Normal University, 637009 Nanchong, People's Republic of China

<sup>2</sup>National Astronomical Observatories, Chinese Academy of Sciences, 100012 Beijing, People's Republic of China

<sup>3</sup>Physics Department, Xiangtan University, 411105 Xiangtan, People's Republic of China

<sup>4</sup>Instituto de Astrofísica de Canarias, Vía Láctea, 38205 La Laguna, Tenerife, Spain

<sup>5</sup>Universidad de La Laguna, Departamento de Astrofísica, 38206 La Laguna, Tenerife, Spain

<sup>6</sup>Institute of Space Sciences, School of Space Science and Technology, Shandong University, 264209 Weihai, People's Republic of China

### ABSTRACT

We present a catalog of 486 Ba stars identified in the GALAH DR4 survey using high-resolution spectra and precise abundance measurements. The sample was selected based on *s*-process enrichment criteria involving the abundances of Ba and La relative to Eu, and further refined using the signed-distance method, resulting in the largest sample of Ba stars to date, including five newly identified Ba dwarfs. Using astrometric and kinematic parameters from Gaia DR3 and StarHorse, we derived the Galactic velocity components for 367 Ba stars and found that most belong to the thin or thick disk, while 18 exhibit halo-like kinematics. Chemical abundance analysis suggests that most Ba stars are of in situ origin, whereas two stars (4077588766331013248 and 6692980582560946304) display signatures of accreted populations. The  $E-L_z$  diagram further shows that star 4077588766331013248 lies within the region of substructure ED-8. The observed decline of [Ba/Fe] and [La/Fe] with increasing metallicity implies that *s*-process elements originate from nucleosynthetic sites distinct from those of iron-peak elements, while the decreasing [hs/lr] ratio toward higher metallicity indicates higher neutron-capture efficiency at lower metallicity. Both giant and dwarf Ba stars—except for 6053735173729807872—are confirmed binaries hosting white dwarf companions. Moreover, we estimated the masses of the former asymptotic giant branch (AGB) companions to these Ba stars based on the good agreement between the FRUITY AGB model predictions and their observed abundance patterns.

Keywords: Barium stars (135); Chemical abundances (224); Asymptotic giant branch (108)

### 1. INTRODUCTION

Barium (Ba) stars have long been a subject of considerable interest in stellar astrophysics, as they constitute a class of chemically peculiar giants and dwarfs characterized by overabundances of slow neutron-capture (*s*-process) elements such as Ba, La, Ce, and Nd (Bidelman & Keenan 1951; Burbidge et al. 1957). They typically span spectral types from G to K, with effective temperatures of 4000–6000 K. The peculiar chemical patterns of these stars have long attracted attention, as they cannot be explained by standard stellar evolution. It is widely accepted that *s*-process elements are synthesized in low- and intermediate-mass stars with  $M \sim 1.3\text{--}8 M_\odot$  during the asymptotic giant branch (AGB) phase, following the red giant stage (Gallino et al. 1998; Busso et al. 1999; Käppeler et al. 2011). Early studies of radial-velocity variations revealed that many Ba stars are members of binary systems, with unseen white dwarf (WD) companions that were formerly AGB stars (McClure et al. 1980; McClure & Woodsworth 1990; Han et al. 1995; Jorissen et al. 1998, 2019). Mass transfer from these companions is believed to be the primary mechanism for the observed *s*-process enrichment, highlighting the close connection between chemical peculiarities, AGB stars, and binary evolution (Cseh et al. 2018; Roriz et al. 2021a,b; Stancliffe 2021; Goswami & Goswami 2023; Roriz et al. 2024).

\* Contact e-mail: gcyang@nao.cas.cn

† Contact e-mail: zjk@nao.cas.cn

‡ Contact e-mail: nian@cwnu.edu.cn

Historically, the study of Ba stars has progressed from initial spectroscopic identifications (e.g., Warner 1965; Lu 1983, 1991) to detailed abundance analyses (e.g., Začs 1994; Liang et al. 2000, 2003; Liu et al. 2009). Systematic catalogs and high-resolution spectroscopic observations have allowed researchers to investigate correlations between stellar atmospheric parameters, elemental abundances, and companion masses (Allen & Barbuy 2006a,b; Pereira et al. 2011; de Castro et al. 2016; Yang et al. 2016; Karinkuzhi et al. 2018; Yang et al. 2024). These studies showed that the degree of *s*-process enhancement is consistent with nucleosynthesis in AGB stars and depends on the properties of the binary system, such as orbital separation and companion mass. In addition, variations in the ratios of light (e.g., Sr, Y, and Zr) to heavy (e.g., Ba, La, Ce, and Nd) *s*-process elements provide insights into the efficiency of neutron-capture processes and material accretion, offering a valuable probe of AGB nucleosynthesis and binary interaction mechanisms (de Castro et al. 2016; Cseh et al. 2018; Roriz et al. 2021a,b).

Compared to the relatively large samples of Ba giants analyzed through high-resolution spectroscopy—for instance, 169 and 180 stars reported by de Castro et al. (2016) and Roriz et al. (2021a), respectively—the number of Ba dwarfs confirmed from detailed chemical analyses remains small, with only about 71 identified to date (e.g., Kong et al. 2018; Purandardas et al. 2019; Shejeelammal et al. 2020; Liu et al. 2021; Karinkuzhi et al. 2021b; Roriz et al. 2024). Despite decades of observational and theoretical efforts, the total number of Ba stars in the Galaxy remains uncertain. Han et al. (1995) estimated that up to 22,000 Ba stars with  $V \leq 10.0$  may exist in the Milky Way. Thanks to the extensive datasets delivered by the large-scale spectroscopic surveys such as the Large Sky Area Multi-Object Fiber Spectroscopic Telescope (LAMOST; Cui et al. 2012; Zhao 2012) and Galactic Archeology with HERMES (GALAH; De Silva et al. 2015; Sheinis et al. 2015; Bunder et al. 2024), it has become feasible to conduct systematic and large-scale searches for Ba stars (Norfolk et al. 2019; Rekhi et al. 2024; Chen et al. 2025). Moreover, detailed chemical abundance patterns, particularly for neutron-capture elements, show substantial diversity. Since the nucleosynthetic processes operating in AGB stars are not yet fully understood, large homogeneous spectroscopic surveys now provide an essential means to investigate Ba stars systematically, increasing both sample sizes and the precision of abundance measurements.

In this study, we present a comprehensive analysis of Ba stars based on the fourth data release (DR4) of the GALAH survey (Bunder et al. 2024), providing a catalog of 486 stars with well-determined stellar parameters. We examined their elemental abundance patterns, focusing on *s*-process enrichment, and investigate their kinematic properties to explore connections between chemical peculiarities and Galactic dynamics. Our analysis aims to provide new insights into the formation history, binary evolution, and chemical characteristics of Ba stars. The structure of this paper is organized as follows. Section 2 outlines the data selection and methodology. Section 3 presents the analysis of the kinematic properties, progenitor systems, chemical abundances, and binarity of the Ba stars. Finally, Section 4 summarizes the main conclusions.

## 2. DATA AND METHODS

In this study, we utilized data from the GALAH DR4 survey (Bunder et al. 2024), which provides high-resolution ( $R \sim 28,000$ ) optical spectra for 917,588 stars observed with the HERMES spectrograph on the 3.9 m Anglo-Australian Telescope. The catalog delivers homogeneous estimates of stellar atmospheric parameters ( $T_{\text{eff}}$ ,  $\log g$ ,  $[\text{Fe}/\text{H}]$ , and  $\xi_t$ ) along with abundances for up to 32 chemical species. Such a large and uniform data set offers unprecedented opportunities to probe the chemical enrichment and dynamical history of the Milky Way, while also informing broader investigations into the origin of elements and the stellar evolution. To enhance our analysis, we complemented the GALAH spectroscopy with high-precision astrometry from Gaia DR3 (Gaia Collaboration et al. 2023) and distance constraints from the StarHorse catalog (Queiroz et al. 2023).

We adopted the standard convention for elemental abundances. For an element  $i$ , its absolute abundance is defined as  $A(i) = \log_{10}(N_i/N_{\text{H}}) + 12$ , where  $N_i$  and  $N_{\text{H}}$  are the number densities of element  $i$  and hydrogen, respectively. Based on the measured abundance ratios  $[i/\text{Fe}]$  and  $[\text{Fe}/\text{H}]$ , we derived the absolute abundance as  $A_{i,*} = [i/\text{Fe}] + [\text{Fe}/\text{H}] + A_{i,\odot}$ , where  $A_{i,\odot}$  is the adopted solar photospheric abundance from Asplund et al. (2009).

To ensure the reliability of our sample, we first applied quality flags in GALAH DR4 to exclude stars with unreliable stellar parameters or elemental abundances. Ba and La are taken as representative *s*-process elements, whereas Eu is considered a typical *r*-process element, primarily produced in core-collapse supernovae or neutron star mergers (Beers & Christlieb 2005; Qian & Wasserburg 2007; Abbott et al. 2017; Stancliffe 2021). Following the classification scheme of Beers & Christlieb (2005), we retained stars with  $[\text{Ba}/\text{Eu}] > 0.5$  and  $[\text{La}/\text{Eu}] > 0.5$ , indicative of *s*-process enrichment. Subsequently, candidate Ba stars were identified using the  $[s/\text{Fe}]$  ratio, defined following the criteria of de Castro et al. (2016). The  $[s/\text{Fe}]$  ratio, defined as the mean abundance of several main *s*-process elements—including not only

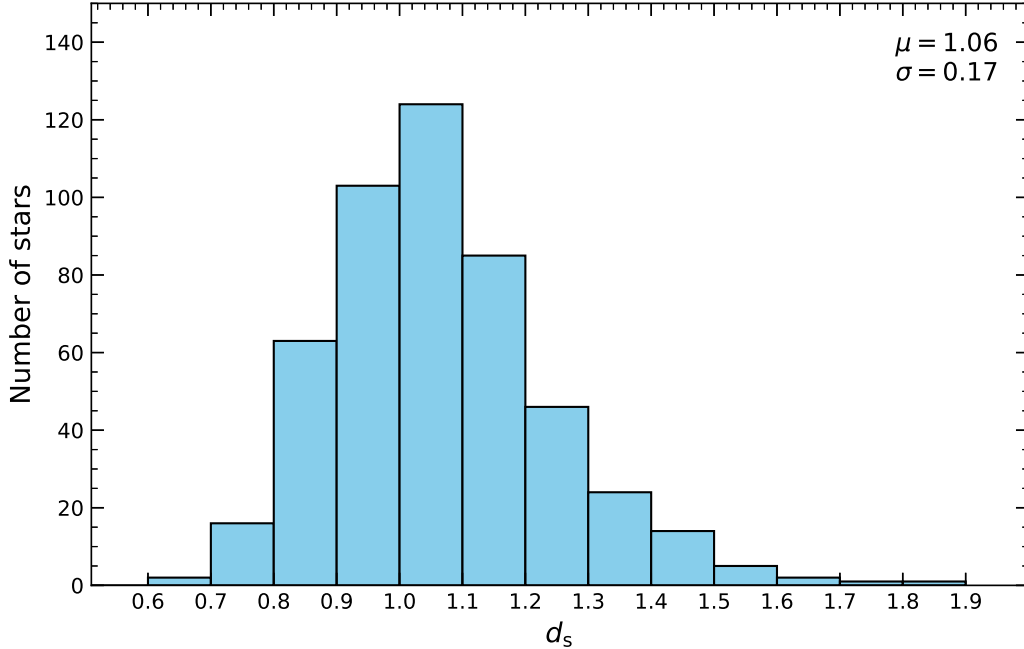


Figure 1. Distribution of the  $d_s$  distances for the Ba stars in our sample. The corresponding mean ( $\mu$ ) and standard deviation ( $\sigma$ ) are indicated in the figure.

Ba and La but also Sr, Y, Zr, Ce, and Nd—relative to Fe (de Castro et al. 2016), serves as a primary diagnostic for  $s$ -process enrichment. Stars with  $[s/\text{Fe}]$  values significantly higher than typical field stars are classified as  $s$ -rich. Various thresholds have been proposed, ranging from  $[s/\text{Fe}] = 0.34$  (Rojas et al. 2013) down to 0.25 (de Castro et al. 2016). In this work, we adopted the latter threshold, consistent with Yang et al. (2024), as the first-step selection criterion for Ba star candidates.

As a second-step verification, we employed the methodology of Karinkuzhi et al. (2021a), who suggested a signed distance,  $d_s$ , to quantify the deviation of a star’s abundance pattern from the solar  $r$ -process composition:

$$d_s = \frac{1}{N} \sum_{i=1}^N (A_{i,*} - A_{i,r,\odot}), \quad (1)$$

where  $A_{i,r,\odot}$  is the solar  $r$ -process abundance from Goriely (1999), scaled to match the Eu abundance of the target star. The element set considered is  $i = \text{Sr, Y, Zr, Ba, La, Ce, Nd}$ . In this scheme,  $d_s$  increases with higher  $s$ -process enrichment, reflecting a stronger deviation from the solar  $r$ -process pattern. Following Karinkuzhi et al. (2021a), we adopted  $d_s = 0.6$  as the threshold for Ba stars and used this criterion to perform a second-step verification of the selected candidates. As a result, the number of Ba star candidates decreased from 488 to 486, with two stars (3419017310212847488 and 3308913761994892672) showing  $[s/\text{Fe}] > 0.25$  but lacking reliable  $d_s$  values due to unreliable  $[\text{Fe}/\text{H}]$  determinations. The distribution of  $d_s$  for the Ba stars is shown in Figure 1. As illustrated in the figure, the  $d_s$  values of the sample stars range from 0.68 to 1.83, with the distribution peaking at a mean value of  $\mu = 1.06$  and a standard deviation of  $\sigma = 0.17$ .

Based on the computation and selection criteria described above, we constructed a catalog of Ba stars from GALAH DR4. The final catalog contains 486 Ba stars, as listed in Table 1. In this table, stellar identifiers from GALAH DR4, Two Micron All Sky Survey (2MASS), and Gaia DR3 are all provided. Throughout the paper, we adopt the Gaia DR3 source IDs when referring to specific objects. The R.A., decl., stellar masses, atmospheric parameters, and heavy-element abundances are taken from GALAH DR4. The  $V_{JK_s}$  magnitudes of the sample stars are computed using Equation (1) of Bunder et al. (2024), based on the 2MASS  $J$  and  $K_s$  magnitudes. The diagnostic indicators of  $s$ -process

enrichment,  $[s/Fe]$  and  $d_s$ , as well as the inferred AGB companion masses of Ba stars,  $M_{AGB}$ , are derived in this work and discussed in the following sections.

For a clearer view of the distributions of the stellar atmospheric parameters,  $T_{\text{eff}}$ ,  $\log g$ , and  $[Fe/H]$ , we present in Figure 2 the corresponding histograms for the final Ba star sample. As shown in the figure, the sample mainly spans effective temperatures of  $\sim 3500\text{--}5500$  K and surface gravities from  $\log g \approx 1.0$  to 3.0 dex, indicating that the majority of the stars are giants and subgiants. The metallicity distribution peaks around  $[Fe/H] \approx -0.5$ , with a tail extending toward lower metallicities, reflecting the metal-poor nature of a significant fraction of the Ba stars. These distributions provide a global overview of the parameter space covered by our sample.

The distribution of the sample stars in the effective temperature versus surface gravity diagram is shown in Figure 3. The majority of the Ba stars are concentrated along the giant branch with  $\log g < 4.0$  dex. We identify 481 Ba giants out of a total of 475,914 giants in GALAH DR4, corresponding to a fraction of  $\sim 0.1\%$ . This value is lower than the commonly quoted incidence of  $\sim 1\%$  for Ba stars among giant populations reported in previous studies (Williams 1975; Lu 1991; Lebzelter et al. 2013). The discrepancy is primarily due to our conservative selection strategy. To ensure the reliability of the final sample, we applied strict quality flags in GALAH DR4 to exclude stars with unreliable stellar parameters or elemental abundances, which significantly reduces the effective parent sample. In addition, the combined requirements on  $[s/Fe]$  and the signed distance  $d_s$  further restrict the sample to objects with robust  $s$ -process enrichment signatures. As a result, our catalog represents a highly reliable, though incomplete, sample of Ba giants.

Five objects lie on the main sequence and are classified as Ba dwarfs with  $\log g > 4.0$  dex. These newly identified dwarfs—4904639351072483840, 4644665049364988928, 3220808727029495680, 5480510146667329152, and 6810035273351899648—increase the known Ba dwarf population from 71 to 76 (Roriz et al. 2024). Despite the large overall Ba star sample identified in GALAH DR4, the number of Ba dwarfs remains strikingly small compared to that of Ba giants. This imbalance is likely driven by strong observational and evolutionary biases. As discussed by Kong et al. (2018) and Escorza et al. (2017, 2019), Ba dwarfs are intrinsically more difficult to identify because their higher effective temperatures lead to weaker  $s$ -process absorption features, making chemical peculiarities less conspicuous than in cooler giants. In addition, the relatively shallow convective envelopes of main-sequence stars can dilute the accreted  $s$ -process material, further reducing observable abundance enhancements. Classical Ba star surveys have also historically focused on luminous G–K giants, introducing a selection bias against dwarfs. Moreover, mass transfer via wind accretion may not yet have occurred or may not always produce immediately detectable chemical signatures during the main-sequence phase, particularly in long-period systems (Escorza et al. 2019).

### 3. ANALYSIS

#### 3.1. Kinematic properties

The kinematic analysis of stars in the solar neighborhood is commonly performed in terms of the three Galactic velocity components  $U$ ,  $V$ , and  $W$ , which are defined as pointing toward the Galactic center, along the direction of Galactic rotation, and toward the north Galactic pole, respectively. Using precise parallaxes, proper motions, and radial velocities from Gaia DR3 (Gaia Collaboration et al. 2023), we computed the full three-dimensional space motions of our sample stars.

The heliocentric space velocities were computed following the prescription of Johnson & Soderblom (1987) and subsequently transformed to the local standard of rest (LSR) using the solar motion vector  $(U_{\odot}, V_{\odot}, W_{\odot}) = (11.1, 12.24, 7.25)$   $\text{km s}^{-1}$  (Schönrich et al. 2010). To ensure the reliability of our sample, we applied the following quality cuts prior to the velocity calculations: (i) stars with a relative parallax error larger than 20% (parallax error/parallax  $> 0.2$ ) are discarded (Carrillo et al. 2024); (ii) distances were computed as the inverse of the Gaia parallaxes whenever available and reliable. For stars with distances exceeding 4 kpc, we adopted StarHorse parallaxes instead of Gaia data; stars lacking both reliable Gaia and StarHorse parallaxes were excluded to maintain the integrity of the results. After these selections, space velocities were derived for a final sample of 367 Ba stars.

Figure 4 presents the Toomre diagram, where the quantity  $(U_{\text{LSR}}^2 + W_{\text{LSR}}^2)^{1/2}$  is plotted against  $V_{\text{LSR}}$ . The semicircular curves mark the canonical boundaries separating the thin- and thick disk populations, corresponding to total velocities  $V_{\text{tot}} = (U_{\text{LSR}}^2 + V_{\text{LSR}}^2 + W_{\text{LSR}}^2)^{1/2}$  of 85 and 180  $\text{km s}^{-1}$ , respectively (Chen et al. 2004). As shown in the figure, the majority of our stars belong to the Galactic thin and thick disks, consistent with the findings of Gómez et al. (1997), Pereira et al. (2011), and Norfolk et al. (2019). In contrast, 18 objects exhibit kinematics characteristic of the Galactic halo. Furthermore, stars with near-solar metallicities are found primarily in the thin and thick disks, whereas those residing in the halo are predominantly metal-poor. The five newly identified Ba dwarfs all have near-solar metallicities and are

Table 1. Properties of the 486 Ba stars.

GALAH ID	2MASS ID	Gaia DR3 ID	R.A. (J2016.0)	Decl (J2016.0)	$V_{\text{HkS}}$ (mag)	$M_{\text{Ba}}$ ( $M_{\odot}$ )	$T_{\text{eff}}$ (K)	$\log g$ (dex)	[Fe/H]	$\xi$ ( $\text{km s}^{-1}$ )	[C/Fe]	[Sr/Fe]	[Y/Fe]	[Zr/Fe]	[Ba/Fe]	[La/Fe]	[Ce/Fe]	[Nd/Fe]	[Sm/Fe]	[Eu/Fe]	[s/Fe]	$d_{\ast}$ ( $M_{\odot}$ )		
210719001601247	00112191-6201326	4904639351072483840	00:11:21.97	-62:01:32.50	13.96	0.72	4490.90	4.60	0.04	0.66	-	0.58	0.33	0.08	0.67	0.92	0.78	0.57	0.33	-0.02	0.56	1.12	1.5	
200905003101166	00150916-6657084	4707537593846950528	00:15:09.16	-66:57:08.61	12.32	0.95	4380.84	2.04	-0.53	1.52	-0.03	0.05	0.38	0.48	1.02	0.93	0.41	0.67	0.76	0.19	0.56	0.97	3.0	
201005003601167	00303605-6922184	4702688545706197760	00:30:36.10	-69:22:18.41	12.85	0.99	4527.02	2.04	-0.69	1.39	0.2	-	0.58	0.91	1.35	1.37	1.02	1.09	0.68	0.52	1.05	1.02	1.5	
161116002201312	00365219-7311276	4688891117917292544	00:36:52.19	-73:11:27.69	13.94	3.47	4298.13	1.30	-0.57	2.65	0.15	0.16	0.13	0.17	0.58	0.89	-0.36	0.29	0.13	0.00	0.27	0.81	1.3	
140814006001283	00464733-7431422	4685489538152953856	00:46:47.34	-74:31:42.09	13.48	4.01	3867.45	0.52	-0.35	2.69	-	-0.09	-0.24	0.04	0.94	0.48	0.34	0.54	0.29	-0.03	0.29	0.88	3.0	
140807005601363	01112540-7317042	4687174196135131008	01:11:25.40	-73:17:04.31	13.79	1.95	4177.95	1.02	-0.79	2.73	0.21	-	-0.14	-0.13	0.92	0.84	0.60	0.62	0.47	0.28	0.45	0.71	3.0	
151109002101111	01300971+0528538	2564906606055659520	01:30:09.71	+05:28:53.80	12.30	1.09	4895.70	2.45	-0.59	1.69	0.21	-	0.67	0.30	1.25	1.23	1.00	0.94	0.56	0.48	0.90	0.91	1.5	
201001003201189	02074101-6458483	4699880461727404544	02:07:41.01	-64:58:48.40	12.62	1.06	4838.88	2.91	-0.29	1.23	0.05	0.18	0.55	0.32	0.83	0.66	0.62	0.41	0.51	-0.02	0.51	1.10	1.5	
191106003301258	02124334-7323054	4644364539093274496	02:12:43.38	-73:23:05.40	13.69	0.97	4683.97	2.52	-0.48	1.31	0.15	-	0.68	0.33	1.31	1.23	0.89	0.93	1.00	0.48	0.90	0.96	3.0	
140811005601156	02134217-7226579	4644665049364988928	02:13:42.21	-72:26:57.90	13.94	0.65	4250.07	4.55	-0.35	0.78	-	-	0.17	-	0.27	1.07	-	-	0.13	-0.25	0.50	1.17	1.5	
...	...	...	...	...	...	...	...	...	...	...	...	...	...	...	...	...	...	...	...	...	...	...	...	...
...	...	...	...	...	...	...	...	...	...	...	...	...	...	...	...	...	...	...	...	...	...	...	...	...

Note. The star identifiers and the data in columns 4, 5, and 7-21 are taken from the GALAH survey.  
(The complete table is available in machine-readable format.)

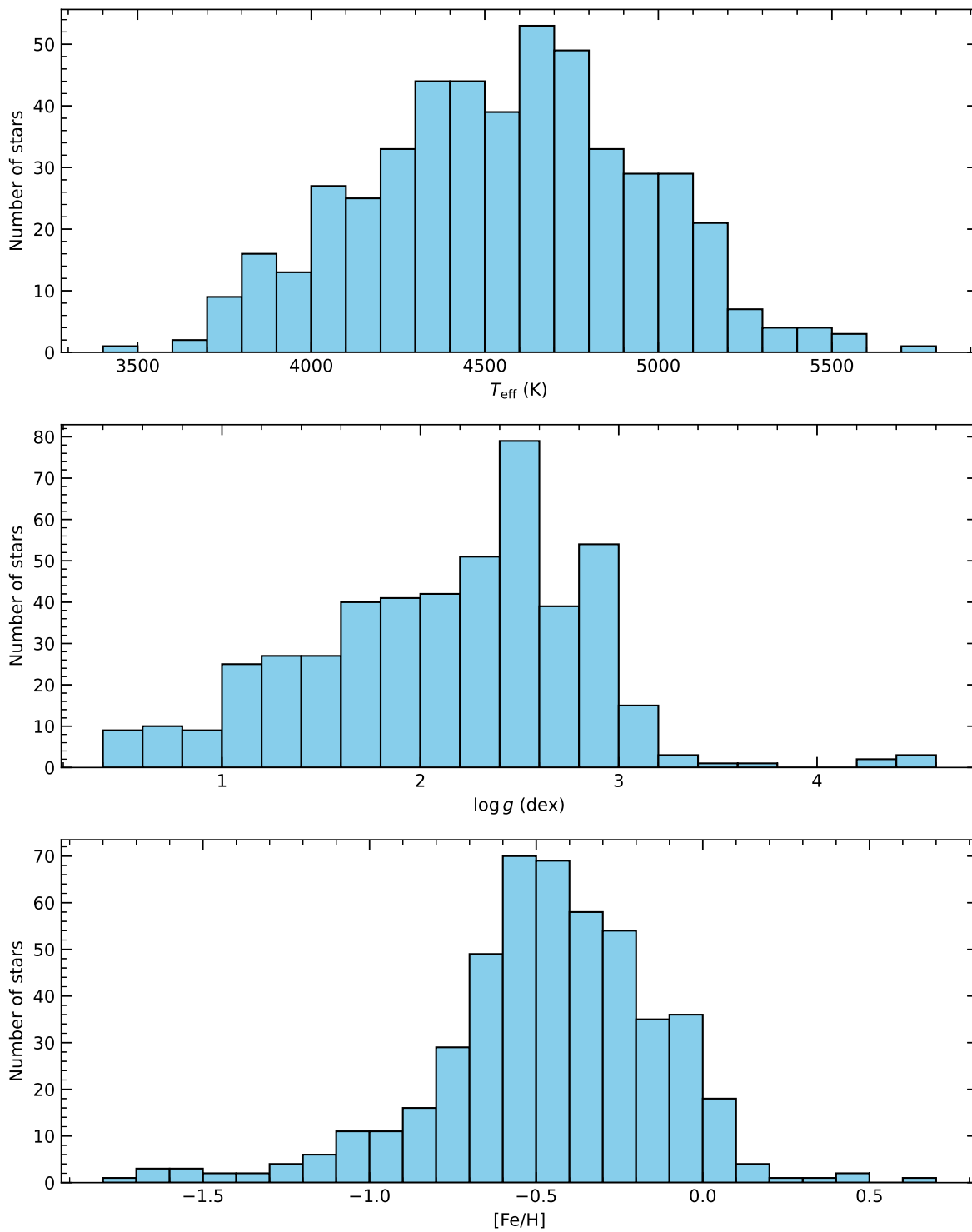


Figure 2. Histograms of  $T_{\text{eff}}$ ,  $\log g$ , and  $[\text{Fe}/\text{H}]$  for the Ba star sample.

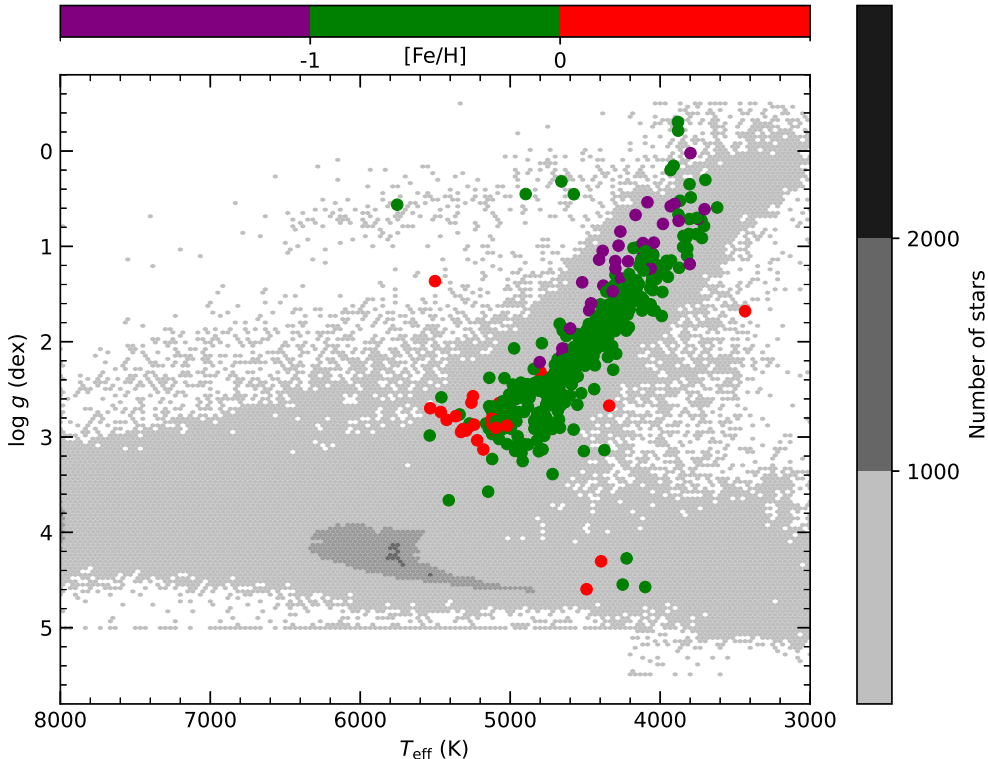


Figure 3. Kiel diagram of Ba stars in GALAH, with points colored according to their metallicities. For reference, all GALAH DR4 stars are plotted in the background as filled gray circles.

located in the thin disk, in agreement with expectations from models of Galactic chemical evolution (Travaglio 2001; Brusadin et al. 2013; Matteucci 2021).

To examine the spatial distribution of the Ba stars, we plot their vertical height ( $Z$ ) as a function of Galactocentric radius ( $R_{gc}$ ) in Figure 5. The  $X$ ,  $Y$ , and  $Z$  Galactocentric coordinates are taken from the GALAH DR4 catalog, with the origin defined at the Galactic center. As expected from our distance cut ( $d < 4$  kpc), the resulting 367 stars are concentrated in the solar neighborhood in the  $Z$ -direction. In contrast to the relatively scattered spatial distribution of the Ba giants, the five Ba dwarfs exhibit a much more concentrated distribution and are all located in the solar neighborhood. Interestingly, 18 stars classified as halo members are located near the solar plane. This may be explained by their current orbital phase, as halo stars can pass through the disk and temporarily reside near  $Z \approx 0$  during their Galactic orbits.

### 3.2. Accreted versus in situ origin

The stars in our Galactic halo preserve the record of its hierarchical assembly, shaped by successive accretion events (Gilmore et al. 2002; Majewski 2017; Laporte et al. 2018). Distinguishing accreted stars from in situ stars is challenging, as debris from ancient mergers is largely phase mixed. Conserved dynamical quantities, particularly angular momentum and orbital energy, combined with stellar chemical abundances, provide a powerful means to identify progenitor systems (Naidu et al. 2020). Large-scale surveys have revealed both well-known structures, such as the Sagittarius and Helmi streams, and recent discoveries like Gaia–Sausage–Enceladus (GSE), demonstrating that past mergers have left discernible kinematic and chemical imprints (Belokurov et al. 2018; Helmi et al. 2018). These chemodynamical signatures thus offer a robust framework for tracing the origin of individual stars (Belokurov et al. 2020; Han et al. 2022; Dodd et al. 2023).

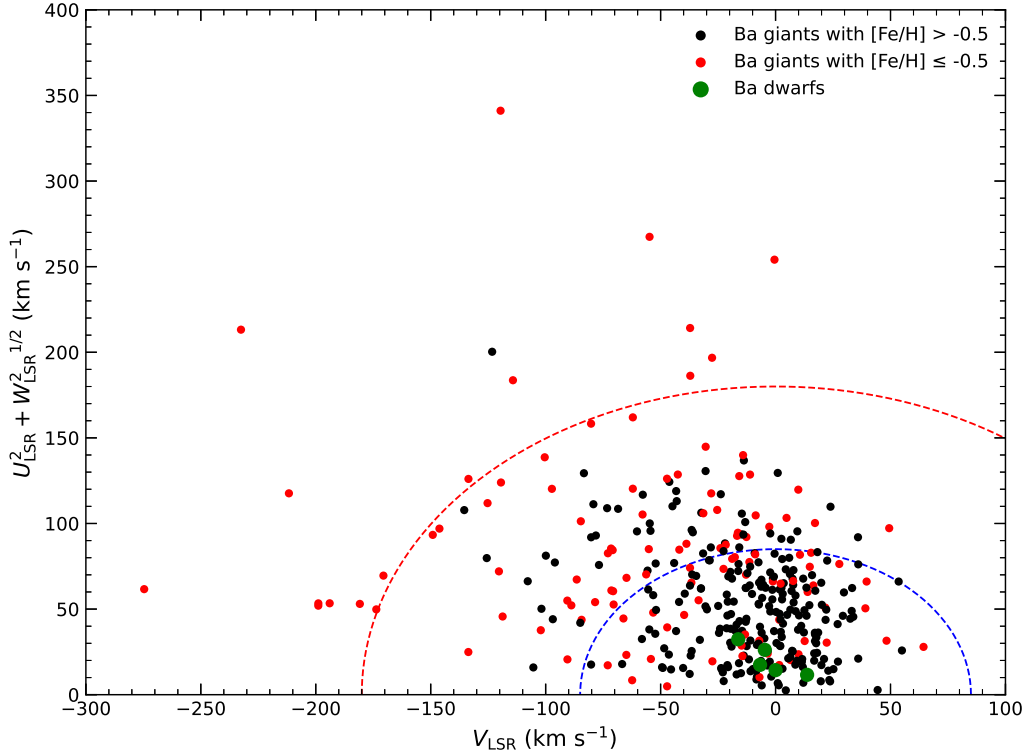


Figure 4. The Toomre diagram of  $(U_{\text{LSR}}^2 + W_{\text{LSR}}^2)^{1/2}$  vs.  $V_{\text{LSR}}$  for our sample stars. Black- and red-filled circles represent Ba giants with near-solar metallicities ( $-0.5 < [\text{Fe}/\text{H}] < 0.64$ ) and subsolar metallicities ( $[\text{Fe}/\text{H}] \leq -0.5$ ), respectively. Green-filled circles denote the five newly identified Ba dwarfs in this work. The semicircular curves indicate the boundaries separating thin-disk, thick-disk, and halo populations, with  $V_{\text{tot}} = (U_{\text{LSR}}^2 + V_{\text{LSR}}^2 + W_{\text{LSR}}^2)^{1/2}$  less than  $85 \text{ km s}^{-1}$  (blue curve) and  $180 \text{ km s}^{-1}$  (red curve), respectively (Chen et al. 2004).

The  $[\text{Mg}/\text{Mn}]$  versus  $[\text{Al}/\text{Fe}]$  plane provides a powerful diagnostic for distinguishing accreted from in situ stellar populations. Mg predominantly traces enrichment from core-collapse supernovae, Mn from Type Ia supernovae (SNe Ia), and Al tends to be under-abundant in stars originating from dwarf galaxies compared to in situ populations (Arcones & Thielemann 2023). Halo stars exhibiting  $[\text{Mg}/\text{Mn}] > 0.25$  and  $[\text{Al}/\text{Fe}] < 0$  are typically linked to accreted systems (Carrillo et al. 2024). Based on the GALAH abundance measurements, Figure 6 illustrates the  $[\text{Mg}/\text{Mn}]$ – $[\text{Al}/\text{Fe}]$  distribution of the halo Ba stars. Most of these stars are consistent with an in situ origin, whereas two of them, 4077588766331013248 and 6692980582560946304, are likely accreted from external systems when abundance uncertainties are taken into account. This finding suggests that they may be remnants of past merger events.

To explore the possible substructure associations of the two likely accreted Ba stars, we determined their locations in the three-dimensional integrals-of-motion space, characterized by orbital energy ( $E$ ) and the  $z$ -component of angular momentum ( $L_z$ ). For comparison, the member-star catalog of different substructures was adopted from Dodd et al. (2023). To ensure consistency, we recalculated the  $E$  and  $L_z$  values for the sample stars of Dodd et al. (2023) using the same method applied to our targets. The astrometric and kinematic parameters (e.g., R.A., decl., distance, proper motion, and radial velocity) for both Dodd et al. (2023) and our sample stars were taken from Gaia DR3 (Gaia Collaboration et al. 2023).

The calculations were performed in the Galactocentric reference frame implemented in Astropy (Astropy Collaboration et al. 2013, 2018, 2022). We adopted a solar position of  $R_{\odot} = 8.21 \text{ kpc}$  (McMillan 2017; Bennett & Bovy 2019) and a solar velocity relative to the LSR of  $(U, V, W)_{\odot} = (11.1, 12.24, 7.25) \text{ km s}^{-1}$  (Schönrich et al. 2010), with  $V_{\text{LSR}} = 233.1 \text{ km s}^{-1}$  (McMillan 2017). The coordinate system is right-handed, such that prograde and retrograde orbits correspond to  $L_z < 0$  and  $L_z > 0$ , respectively. Orbital quantities, including actions, eccentricities, and energies, were computed using Gala with its default MilkyWayPotential (Price-Whelan 2017). The resulting distributions are shown in Figure 7. From the figure, we can see that the Ba star 4077588766331013248 lies within the region of substructure

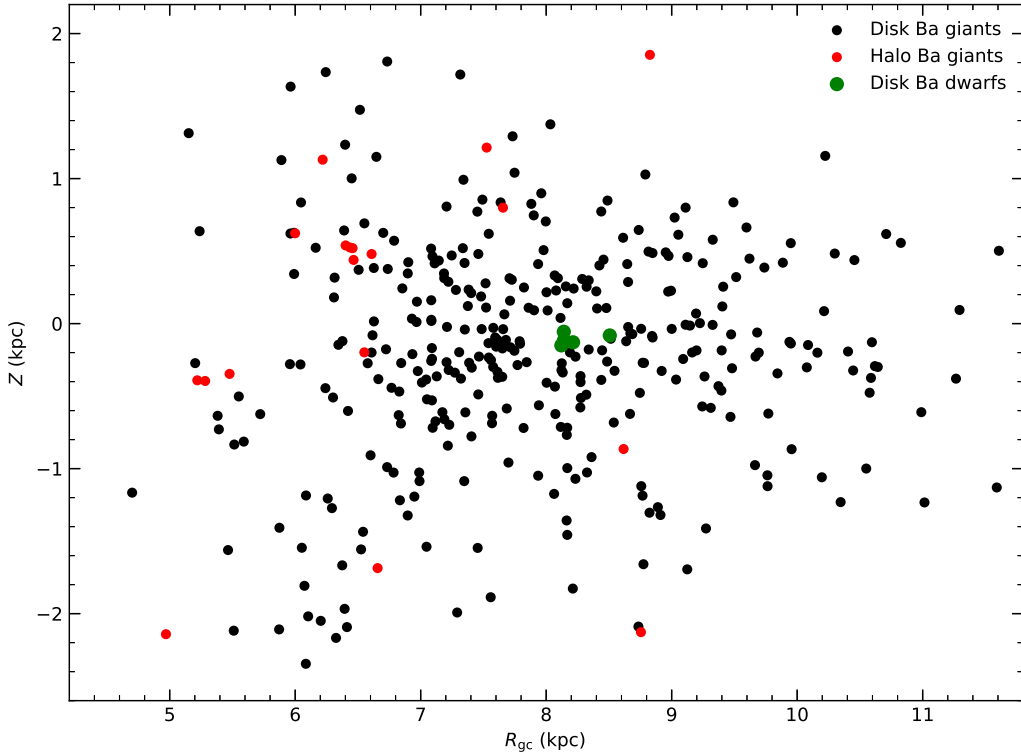


Figure 5. Spatial distribution of the 367 Ba stars, mostly located within 4 kpc, plotted as vertical height versus Galactocentric radius. Filled black and red circles represent Ba giants associated with the Galactic disk and halo, respectively. Filled green circles denote Ba dwarfs.

ED-8 identified by [Dodd et al. \(2023\)](#). This provides additional evidence that this star may have an accreted origin, consistent with the chemical abundance signature shown in Figure 6. For the sample star 6692980582560946304, its location is close to the Helmi streams and ED-1 substructures ([Dodd et al. 2023](#)), or possibly the high- $\alpha$  disk ([Naidu et al. 2020](#)). In this case, the analysis based on Figures 6 and 7 makes it difficult to determine whether the star has an in situ or accreted origin.

### 3.3. Abundances of *s*-process elements and carbon

The chemical abundances of *s*-process elements serve as important tools in studying nucleosynthesis processes and the formation history of Ba stars. Figure 8 shows the  $[i/Fe]$  ratios of two representative *s*-process elements, Ba and La, for the 486 stars in our sample. Most Ba stars exhibit varying degrees of *s*-process overabundance. At  $[Fe/H] \gtrsim -1.0$ , the majority of stars are associated with the Galactic thin and thick disks. As metallicity increases, the  $[i/Fe]$  ratios gradually decline, indicating that *s*-process and iron-peak (e.g., Cr, Mn, Fe, Co, and Ni) elements are not produced in the same astrophysical sites. The *s*-process elements are primarily synthesized in low- and intermediate-mass AGB stars, whereas iron-peak elements are predominantly produced by nuclear fusion in massive stars and SNe Ia ([Snedden et al. 2008](#); [Arcones & Thielemann 2023](#)). At lower metallicities ( $[Fe/H] \lesssim -1.0$ ), the  $[i/Fe]$  ratios drop sharply, likely reflecting the limited contribution of *s*-process nucleosynthesis in the early Galaxy ([Travaglio 1999](#); [Burris et al. 2000](#)). Furthermore, as shown in the figure, the  $[i/Fe]$  ratios of Ba dwarfs show systematic differences compared to the main distribution of Ba giants at similar metallicities. At  $[Fe/H] \lesssim 0$ , Ba dwarfs tend to exhibit lower  $[i/Fe]$  ratios than Ba giants, whereas at  $[Fe/H] \gtrsim 0$ , the trend appears to be reversed. This behavior may suggest that Ba dwarfs and Ba giants have experienced different chemical enrichment histories.

To examine whether there is a radial dependence in the efficiency of *s*-process enrichment among the Ba stars, we investigated the behavior of the  $[s/Fe]$  ratios as a function of Galactocentric radius  $R_{gc}$ . Specifically, we plotted  $[s/Fe]$  versus  $R_{gc}$  and computed the mean  $[s/Fe]$  values in bins of 0.5 kpc in  $R_{gc}$ , as shown in Figure 9. As illustrated in the left panel, the  $[s/Fe]$  ratios display a nearly flat trend with increasing  $R_{gc}$ , with a fitted slope of  $-0.011 \pm 0.008$

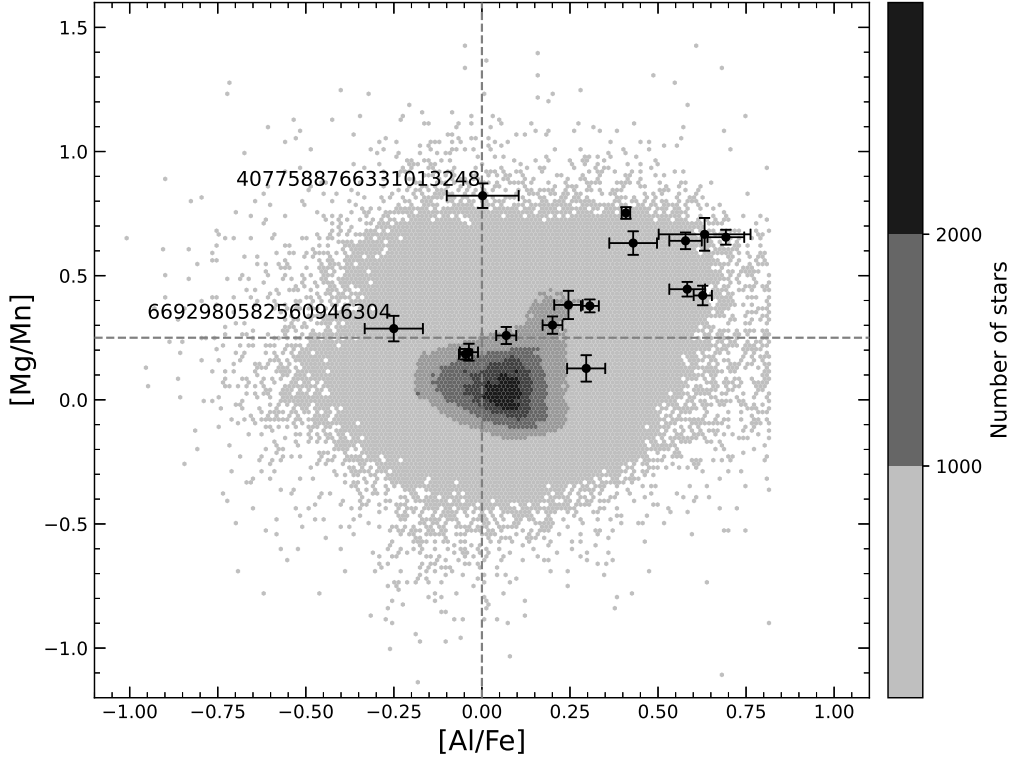


Figure 6.  $[\text{Mg}/\text{Mn}]$  vs.  $[\text{Al}/\text{Fe}]$  for the halo Ba stars (black circles). The vertical and horizontal dashed lines denote  $[\text{Al}/\text{Fe}] = 0$  and  $[\text{Mg}/\text{Mn}] = 0.25$ , respectively. For reference, all GALAH DR4 stars are shown in the background as filled grey circles.

and a large scatter at all radii. The right panel further confirms this result, showing that the mean  $[\text{s}/\text{Fe}]$  values in different  $R_{\text{gc}}$  bins do not exhibit any significant increasing or decreasing trend. Overall, we find no clear evidence for a radial dependence of the  $s$ -process enrichment efficiency within the spatial range probed by our sample. For the five Ba dwarfs, their  $s$ -process enrichment levels are generally lower than the mean value of the Ba giants, and they are all located in the solar neighborhood in terms of Galactocentric radius. Owing to the small number of Ba dwarfs, no firm conclusion can be drawn regarding their radial behavior.

The  $[\text{hs}/\text{ls}]$  ratio, constructed from heavy  $s$ -process (Ba, La, Ce, Nd) and light  $s$ -process (Sr, Y, Zr) elements, serves as a sensitive probe of  $s$ -process efficiency and places strong constraints on AGB nucleosynthesis models. Figure 10 shows  $[\text{hs}/\text{ls}]$  as a function of  $[\text{Fe}/\text{H}]$  for our sample stars. A clear decreasing trend with metallicity is seen, in agreement with previous studies (e.g., Cseh et al. 2018; Roriz et al. 2021b; Yang et al. 2024). A linear fit to the data yields  $[\text{hs}/\text{ls}] = (-0.358 \pm 0.030)[\text{Fe}/\text{H}] + (0.170 \pm 0.017)$ . This trend indicates that heavy  $s$ -process elements dominate the neutron-capture yields at low metallicities ( $[\text{Fe}/\text{H}] < -0.6$ ), while light  $s$ -process elements become more prevalent at higher metallicities (Busso et al. 2001). Negative  $[\text{hs}/\text{ls}]$  values reflect a relative enhancement of light  $s$ -process elements at the corresponding metallicities. The  $[\text{hs}/\text{ls}]$  distributions of Ba dwarfs and Ba giants do not show any obvious systematic differences. However, the present Ba dwarf subsample does not yet allow a statistically robust assessment of potential differences in their  $[\text{hs}/\text{ls}]$  properties.

Furthermore, the  $[\text{hs}/\text{ls}]$  scatter decreases with increasing metallicity, which can be interpreted as a consequence of the gradual homogenization of the interstellar medium over time, driven by the mixing of chemical yields from multiple nucleosynthetic sites, including the main  $s$ -process in AGB stars and the weak  $s$ -process in massive stars (Travaglio 1999; Travaglio et al. 2004).

In addition to the  $s$ -process elements, the abundance behavior of the light element carbon (C) is of particular interest in Ba stars. As a tracer that is highly sensitive to mixing processes during different stages of stellar evolution, carbon provides valuable insight into the nature of the former companion that polluted the Ba stars during its thermally pulsing (TP-) AGB phase (Karinkuzhi et al. 2021b; Roriz et al. 2025). In this work, because reliable carbon abundances are not available for the five Ba dwarfs in GALAH DR4, we focus our analysis on the Ba giants. Using homogeneous

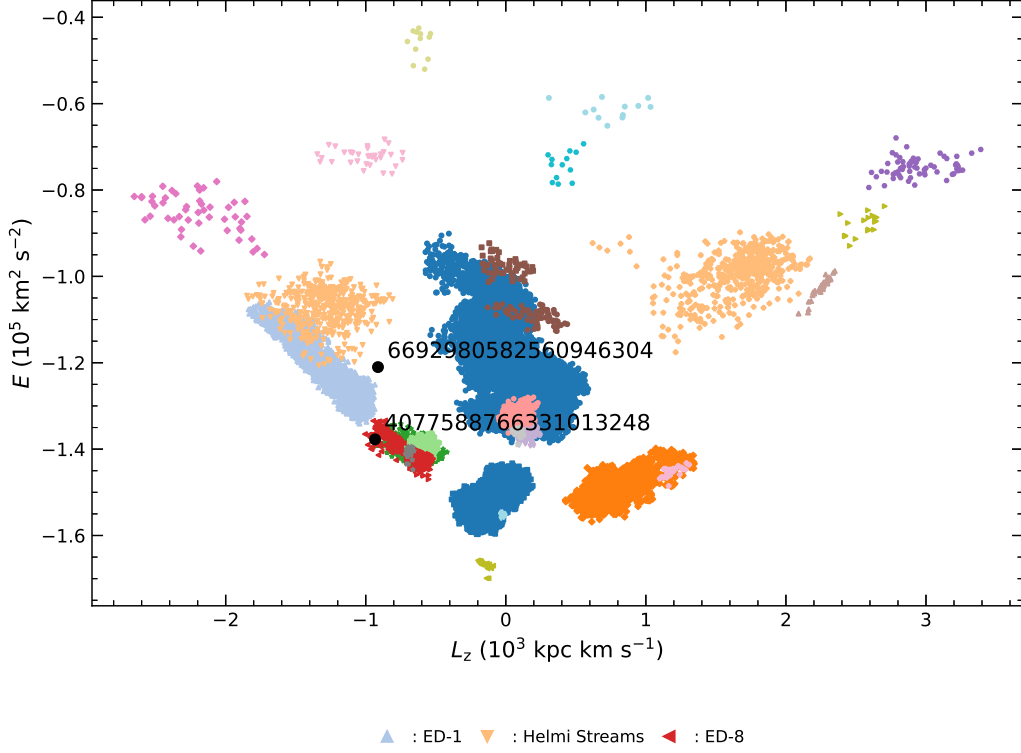


Figure 7.  $E$ - $L_z$  distribution of Galactic halo substructures. Black points mark the positions of our two target stars. Colored points represent different substructures, including Sagittarius, Apeh, GSE, Helmi streams, Thamnos, Sequoia, Arjuna, Ítói, the in situ halo, EDs, and so on (Naidu et al. 2020; Dodd et al. 2023). The substructures located near or overlapping our two sample stars are labeled, illustrating the possible substructure membership of the two Ba stars.

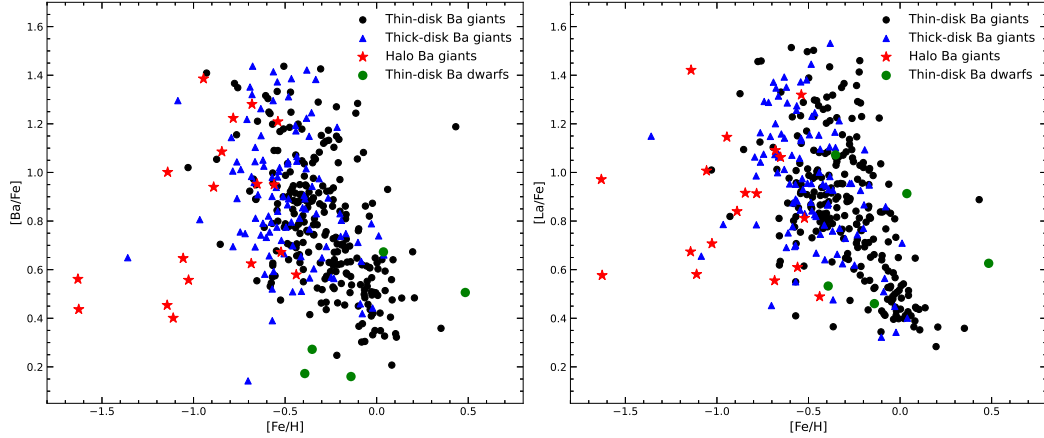


Figure 8. Abundance ratios  $[i/\text{Fe}]$  as a function of  $[\text{Fe}/\text{H}]$  for the two representative  $s$ -process elements, Ba and La, in our Ba stars. Filled black circles, blue triangles, and red stars represent Ba giants belonging to the thin disk, thick disk, and halo, respectively. Filled green circles denote Ba dwarfs.

data from GALAH DR4, we compare the carbon abundances of Ba giants with those of normal giants. As shown in Figure 11, the blue and red curves represent the mean  $[\text{C}/\text{Fe}]$  values in metallicity bins of 0.50 for the Ba giants and normal giants, respectively. The  $[\text{C}/\text{Fe}]$  ratios of Ba giants exhibit an overall decreasing trend with increasing  $[\text{Fe}/\text{H}]$ , in agreement with previous studies (Kong et al. 2018; Roriz et al. 2024). In contrast, the  $[\text{C}/\text{Fe}]$  ratios of normal giants show a weakly increasing or nearly flat trend at  $[\text{Fe}/\text{H}] \gtrsim -1.5$ , consistent with the results of Horta et al. (2023). The

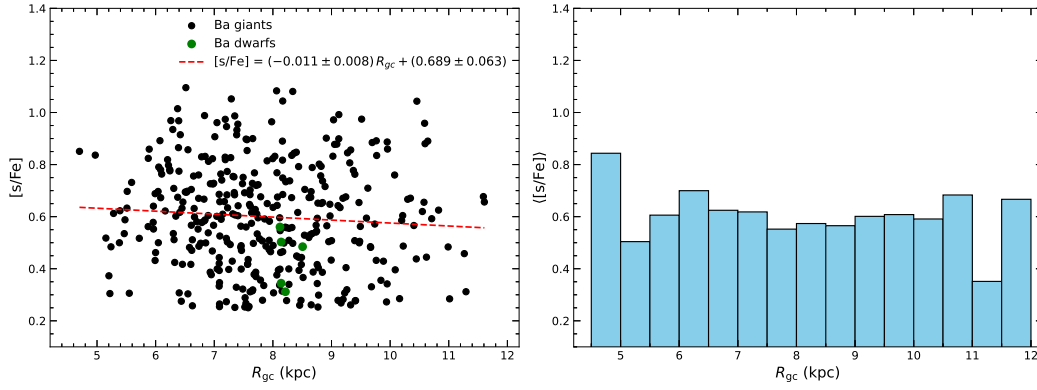


Figure 9. Abundance ratios  $[s/Fe]$  of the Ba stars as a function of Galactocentric radius  $R_{gc}$ . Left panel: individual  $[s/Fe]$  ratios of Ba giants and dwarfs are shown as filled black and green circles, respectively, with the red line indicating the linear fit to the entire sample. Right panel: mean  $[s/Fe]$  values averaged in bins of 0.5 kpc in  $R_{gc}$ .

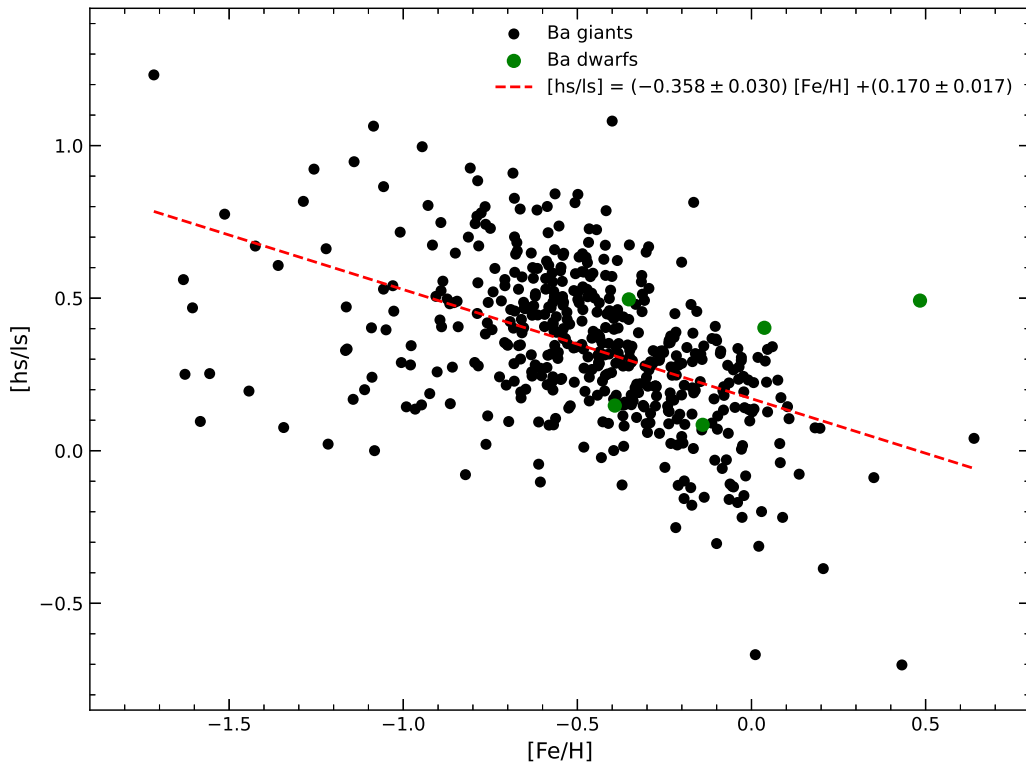


Figure 10. Abundance ratio  $[hs/ls]$  as a function of  $[Fe/H]$  for the Ba star sample. The dashed line represents the best-fit linear regression to the data.

weaker increase in  $[C/Fe]$  at  $[Fe/H] > -1.5$ , compared to lower metallicities, may reflect the increasing contribution of SNe Ia to iron-peak elements without a corresponding production of carbon.

When comparing the mean  $[C/Fe]$  values of Ba giants and normal giants, we find that Ba giants display systematically higher  $[C/Fe]$  ratios at metallicities below  $[Fe/H] \approx -0.3$ , consistent with carbon enrichment through mass transfer from an AGB companion. At higher metallicities, however, the opposite behavior is observed, with Ba giants exhibiting lower  $[C/Fe]$  ratios than normal giants. This metallicity-dependent pattern suggests that carbon enhancement associated with  $s$ -process enrichment is more pronounced at low metallicities, while at higher metallicities it may be diluted by a combination of stellar evolutionary mixing and the increased iron enrichment from SNe Ia. Over the full metallicity

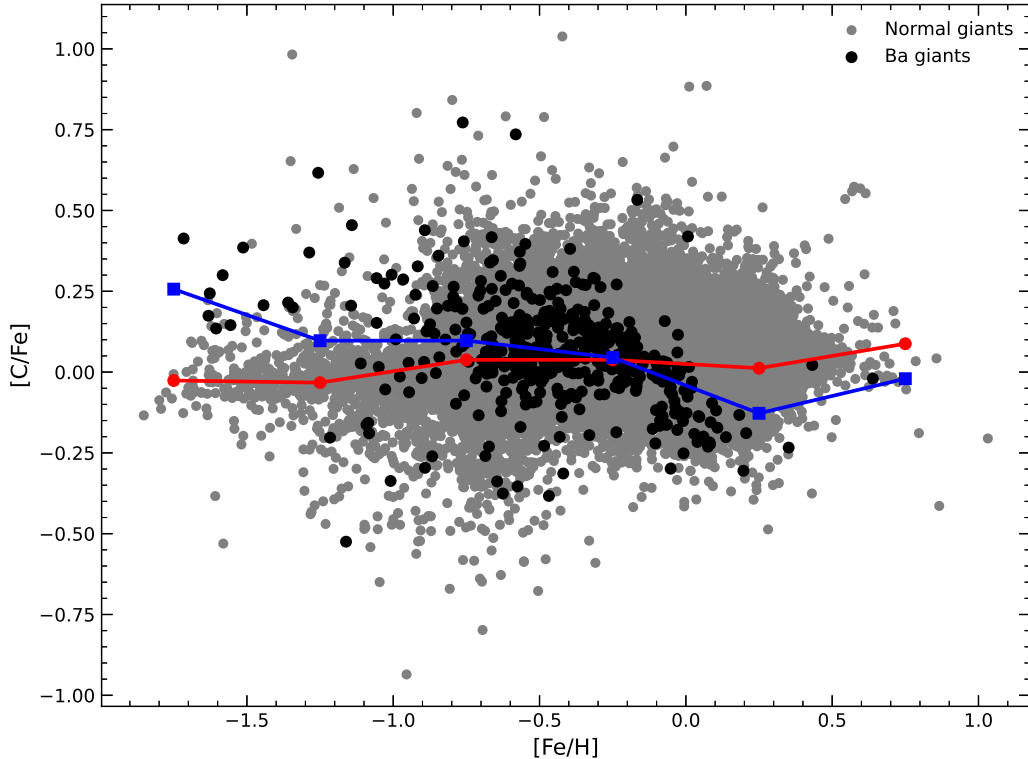


Figure 11. Abundance ratio  $[C/Fe]$  as a function of  $[Fe/H]$  for the Ba giants (black circles) and normal giants (filled gray circles). The blue and red curves refer to the average  $[C/Fe]$  ratios in metallicity bins of 0.50 for Ba giants and normal giants, respectively.

range, the average  $[C/Fe]$  of the Ba giants is higher than that of the normal giants by approximately  $\sim 0.04$ , which is significantly smaller than the enhancement reported by Roriz et al. (2025).

### 3.4. Binarity

In our sample, the Ba giants and dwarfs are not sufficiently evolved to undergo internal  $s$ -process nucleosynthesis, and are therefore considered products of binary (or possibly triple) interactions. Ba stars are thought to form when a former AGB companion—now a WD—enriches the primary star with  $s$ -process material through mass transfer. Using spectral residual analysis, Bunder et al. (2024) searched for binary signatures among GALAH DR4 targets and flagged likely binary systems by reporting the radial velocity of the primary source ( $rv\_comp\_1$ ) and of the potential secondary source ( $rv\_comp\_2$ ) in the catalog. Among our 486 Ba stars, only 74 have measured  $rv\_comp\_2$  values. To further investigate binarity, we compared the radial velocities from GALAH DR4 with those from Gaia DR3. Stars with velocity residuals exceeding the combined observational uncertainties were classified as showing significant radial-velocity variability. Unfortunately, only 271 stars in our sample exhibit such variations.

Although radial-velocity monitoring is an important diagnostic for confirming the binarity of Ba stars, it can be challenging to detect. This difficulty may arise from long orbital periods (Escorza et al. 2019, 2020; Jorissen et al. 2019), nearly pole-on configurations, or highly eccentric orbits where significant velocity changes occur only over a small fraction of the orbital phase (Pourbaix et al. 2004; de Castro et al. 2016). Ultraviolet (UV) photometric excess in the spectral energy distribution (SED) of a star can serve as an indicator of a WD companion (Böhm-Vitense et al. 2000; Shetye et al. 2020). We constructed SEDs for our Ba stars using the Virtual Observatory SED Analyser (VOSA; Bayo et al. 2008) to search for near-UV (NUV; centered at 2271 Å) excess and thereby diagnose the presence of WD companions.

Prior to this analysis, we employed the IDL-based code KMOD, which is widely used in stellar abundance studies (e.g., Mészáros & Prieto 2013; Yong et al. 2013), to interpolate the ATLAS9 model atmosphere grid (Castelli & Kurucz 2004). This interpolation provided the atmospheric model corresponding to the target stellar parameters. Using these

models, we generated synthetic spectra with SPECTRUM (Gray & Corbally 1994). For the input chemical composition, the abundances of neutron-capture elements were adopted from GALAH DR4, as they often differ significantly from solar values, whereas abundances of lighter elements (up to the iron-peak) were kept at solar values (Asplund et al. 2009).

Using these synthetic templates, we evaluated the NUV fluxes of all 486 Ba stars and found significant NUV excesses in all five Ba dwarfs and in nearly the entire Ba giant sample. Figure 12 presents three representative examples (one Ba dwarf, 4904639351072483840, and two Ba giants, 4707537593846950528 and 2564906606055659520), showing the GALEX NUV measurements (Bianchi et al. 2017) together with photometry in additional bands (e.g.,  $U$ ,  $B$ ,  $V$ ,  $u$ ,  $v$ ,  $g$ ,  $b$ , and  $y$ ) from surveys such as CAHA, Generic, Sloan Digital Sky Survey (SDSS), and others for comparison. The optical photometry at wavelengths longer than 3400 Å closely follows the model spectrum, indicating no flux excess in these bands. In contrast, the observed GALEX NUV flux is clearly higher than predicted by the model, providing further evidence that these stars host WD companions, consistent with the widely accepted formation scenario for Ba stars. As shown in the four panels of the figure, the NUV excesses observed in the SEDs of Ba dwarfs exhibit characteristics similar to those seen in Ba giants.

Six stars, however, show no obvious NUV excess. Among them, 4657277066293133056, 3317356770048876672, 6090437043630921472, 4285878256152184832, and 4199611978282443264 can still be classified as binaries based on the presence of the  $rv\_comp\_2$  flag or on detectable radial-velocity variations between GALAH DR4 and Gaia DR3 (see Table B1 in Bunder et al. 2024). For the Ba giant 6053735173729807872, no convincing evidence of binarity is found. Its orbit or geometric configuration may be unfavorable for detection, or the effective temperature of a potential WD companion may be too low to produce a measurable NUV excess. If the star is truly single, the origin of its Ba and La overabundances requires further investigation.

### 3.5. Companion mass estimates

Based on nucleosynthesis models of low-mass stars, Cristallo et al. (2011) investigated the  $s$ -process in AGB stars and developed the FRUITY database. Their models cover stellar masses of 1.3–6.0  $M_{\odot}$  and metallicities from  $Z = 10^{-5}$  to  $3 \times 10^{-2}$ . In these models, the main neutron source is assumed to be the radiative burning of  $^{13}\text{C}$ , and the efficiency of the third dredge-up (TDU) decreases with increasing metallicity. For a given metallicity, the surface enrichment is determined primarily by the amount of dredged-up material and the depth of the convective envelope.

In this work, we inferred the masses of the Ba star companions by comparing the observed neutron-capture element abundances of our sample with the predictions from the FRUITY AGB nucleosynthesis models. Direct comparison with model yields is not straightforward, as the transferred material from the former AGB companion becomes diluted in the envelope of the Ba star. This dilution is driven by both the mass-transfer process itself and subsequent internal mixing, primarily during the first dredge-up. The degree of dilution can be expressed as  $\text{dil} = (M_{\text{AGB,trans}} + M_{\text{Ba,env}})/M_{\text{AGB,trans}}$  (Bisterzo et al. 2012), where  $M_{\text{AGB,trans}}$  is the mass accreted from the companion and  $M_{\text{Ba,env}}$  is the mass of the Ba star’s envelope.

The abundance patterns of AGB models were computed for each Ba star using the approach described by Cseh et al. (2022). For a given element, the diluted abundance,  $[\text{X}/\text{Fe}]_{\text{dil}}$ , was obtained using

$$[\text{X}/\text{Fe}]_{\text{dil}} = \log \left( 10^{[\text{X}/\text{Fe}]_{\text{ini}}} (1 - \delta) + 10^{[\text{X}/\text{Fe}]_{\text{AGB}}} \delta \right), \quad (2)$$

where  $[\text{X}/\text{Fe}]_{\text{ini}}$  denotes the initial abundance ratio, and  $[\text{X}/\text{Fe}]_{\text{AGB}}$  corresponds to the post-AGB yields predicted by the models. The dilution factor  $\delta$  ( $=1/\text{dil}$ ) was determined by scaling the model  $[\text{Ba}/\text{Fe}]$  ratio to match that of the observed star, which is different from Cseh et al. (2022), who derived the  $\delta$  values by scaling the model  $[\text{Ce}/\text{Fe}]$  ratio to the observed  $[\text{Ce}/\text{Fe}]$ . This factor was then applied to compute  $[\text{X}/\text{Fe}]_{\text{dil}}$  for all other elements. To identify the most representative model for each Ba star, we first restricted the comparison to AGB models with metallicities close to that of the star, and subsequently minimized the  $\chi^2$  difference between the observed and model-predicted abundances. Solutions with  $\delta < 1$  were retained, since  $\delta = 1$  would correspond to a physically implausible case of pure, unmixed AGB ejecta.

As illustrative cases, Figure 13 presents the abundance pattern comparisons between the three selected Ba stars and their corresponding best-fit AGB models. The diluted yields from AGB stars of the inferred masses reproduce the observed elemental distributions remarkably well. The inferred companion masses for the entire sample are summarized in Table 1 (column 24). Their distribution across different mass intervals is shown in Figure 14, which highlights that the majority of Ba star companions are low-mass ( $M = 1.5\text{--}3.5 M_{\odot}$ ) TP-AGB stars. These findings align well with

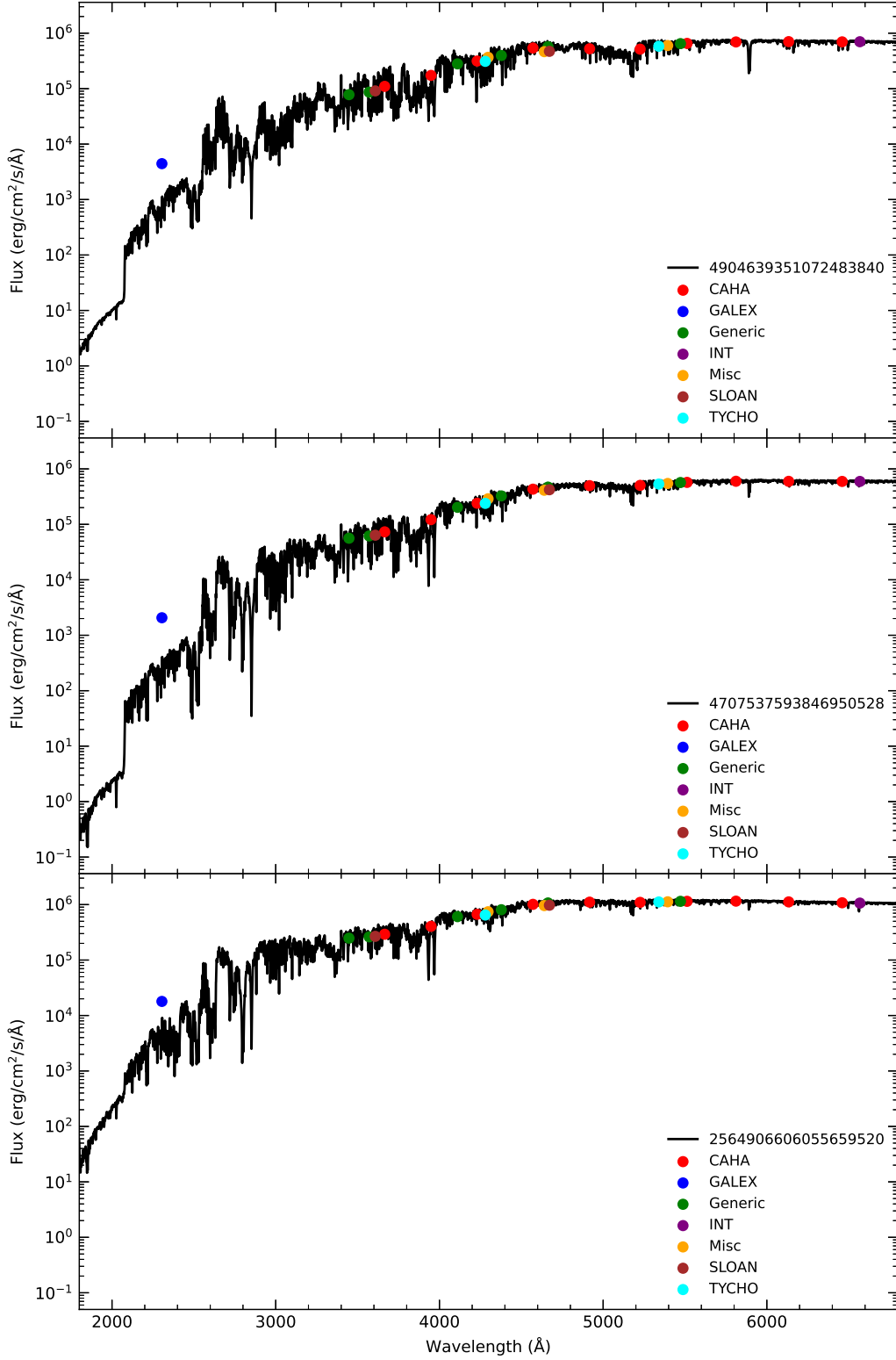


Figure 12. SEDs of one Ba dwarf (4904639351072483840) and two Ba giants (4707537593846950528 and 2564906606055659520), shown as illustrative examples and constructed using VOSA. The NUV photometric data are from GALEX, shown as filled blue circles in the figure. For comparison, photometric measurements in other bands, including those from CAHA, SDSS, and additional surveys, are also plotted. The model spectra are taken from the ATLAS9 grid of stellar atmospheres.

previous studies (e.g., Allen & Barbuy 2006a; Cseh et al. 2018; Goswami & Goswami 2023; Roriz et al. 2024), reinforcing the view that such low-mass AGB stars are the dominant polluters in Ba star systems.

Nevertheless, as shown in Table 1 and Figure 14, there are 93 Ba stars—comprising two Ba dwarfs and 91 Ba giants—whose inferred companion masses exceed  $5.0 M_{\odot}$ , despite the majority of the sample being consistent with pollution by low-mass AGB companions. This result suggests that intermediate-mass stars evolving through the AGB phase and producing  $s$ -process elements may also contribute to the chemical enrichment of Ba binaries, in agreement with previous studies (e.g., Jorissen et al. 2019; Roriz et al. 2021a; Cseh et al. 2022). In addition, we note that a small number of systems exhibit inferred AGB companion masses that are smaller than the present masses of the Ba stars ( $M_{\text{AGB}} < M_{\text{Ba}}$ ). The companion masses estimated in this work correspond to the initial masses of the former AGB stars, inferred by fitting the observed  $s$ -process abundance patterns with the FRUITY AGB nucleosynthesis models, rather than to their present-day remnant masses. During binary evolution, mass transfer through Roche-lobe overflow and/or wind mass accretion can substantially increase the mass of the initially less massive star. As a consequence, a mass-ratio reversal may occur, such that the initially more massive star (the AGB progenitor) becomes less massive after losing most of its envelope, while the initially less massive star (now observed as the Ba star) gains mass and becomes the more massive component. Recent three-dimensional hydrodynamical simulations of Roche-lobe overflow by Ryu et al. (2025) further suggest that the present-day mass ordering of binary components may not necessarily reflect their initial masses, particularly in systems that have undergone substantial mass exchange. Consequently, cases in which the inferred AGB progenitor mass is comparable to or even lower than the current mass of the Ba star may plausibly reflect the evolutionary history of mass transfer in these systems.

#### 4. CONCLUSIONS

In this work, we identified a sample of 486 Ba stars from the GALAH DR4 dataset using high-resolution spectra and precise abundance measurements. The sample was constructed based on the enhancement criteria involving typical  $s$ -process elements (Ba and La) relative to the  $r$ -process element (Eu), as proposed by Beers & Christlieb (2005), and the  $[\text{s}/\text{Fe}]$  criterion by de Castro et al. (2016). To further ensure the purity of the Ba star sample, we applied the signed distance method proposed by Karinkuzhi et al. (2021a) to remove possible non-Ba contaminants. Based on the above methodology, we obtained the largest Ba star sample to date. By presenting the distribution of  $T_{\text{eff}}$  versus  $\log g$ , we identified five new Ba dwarfs (4904639351072483840, 4644665049364988928, 3220808727029495680, 5480510146667329152, and 6810035273351899648), significantly expanding the previously small known population of such objects. Based on this large Ba star sample, we analyzed their kinematic properties, progenitor systems,  $s$ -process abundance characteristics, and binarity. Our main conclusions are as follows:

1. Using reliable parallaxes, proper motions, and radial velocities from Gaia DR3 and StarHorse, we derived the three Galactic velocity components ( $U$ ,  $V$ ,  $W$ ) for 367 Ba stars. Most of these stars belong to the thin or thick disk populations, while a small subset (18 stars) exhibits halo-like kinematics. Stars with near-solar metallicities are mainly distributed within the Galactic disk, whereas the halo members are predominantly metal-poor. The five newly identified Ba dwarfs are characterized by near-solar metallicities and thin-disk kinematics, consistent with Galactic chemical evolution models. The spatial distribution of the 367 Ba stars further shows that the 18 halo objects are located near the solar neighborhood, likely because they are currently passing through the disk near the sun along their Galactic orbits.
2. To investigate whether the halo Ba stars originated from accreted systems or formed in situ, we analyzed their chemical abundances. Using the criteria of  $[\text{Mg}/\text{Mn}] > 0.25$  and  $[\text{Al}/\text{Fe}] < 0$ , which are typically associated with accreted populations (Carrillo et al. 2024), we found that most Ba stars in our sample are likely of in situ origin. However, considering abundance uncertainties, two stars—4077588766331013248 and 6692980582560946304—appear to be consistent with accreted populations. By combining our data with the substructure catalog of Dodd et al. (2023), we further calculated the orbital angular momentum and total energy for these two stars. The star 4077588766331013248 is located within the region of substructure ED-8 identified by Dodd et al. (2023), supporting an external (accreted) origin. In contrast, for 6692980582560946304, its position in the  $E$ - $L_z$  diagram makes it difficult to clearly distinguish between an in situ and an accreted origin.
3. Enrichment in the  $s$ -process elements Ba and La is ubiquitous among the samples, though to varying degrees. The decline of  $[\text{Ba}/\text{Fe}]$  and  $[\text{La}/\text{Fe}]$  ratios toward higher metallicities ( $[\text{Fe}/\text{H}] \gtrsim -1.0$ ) suggests that the  $s$ -process

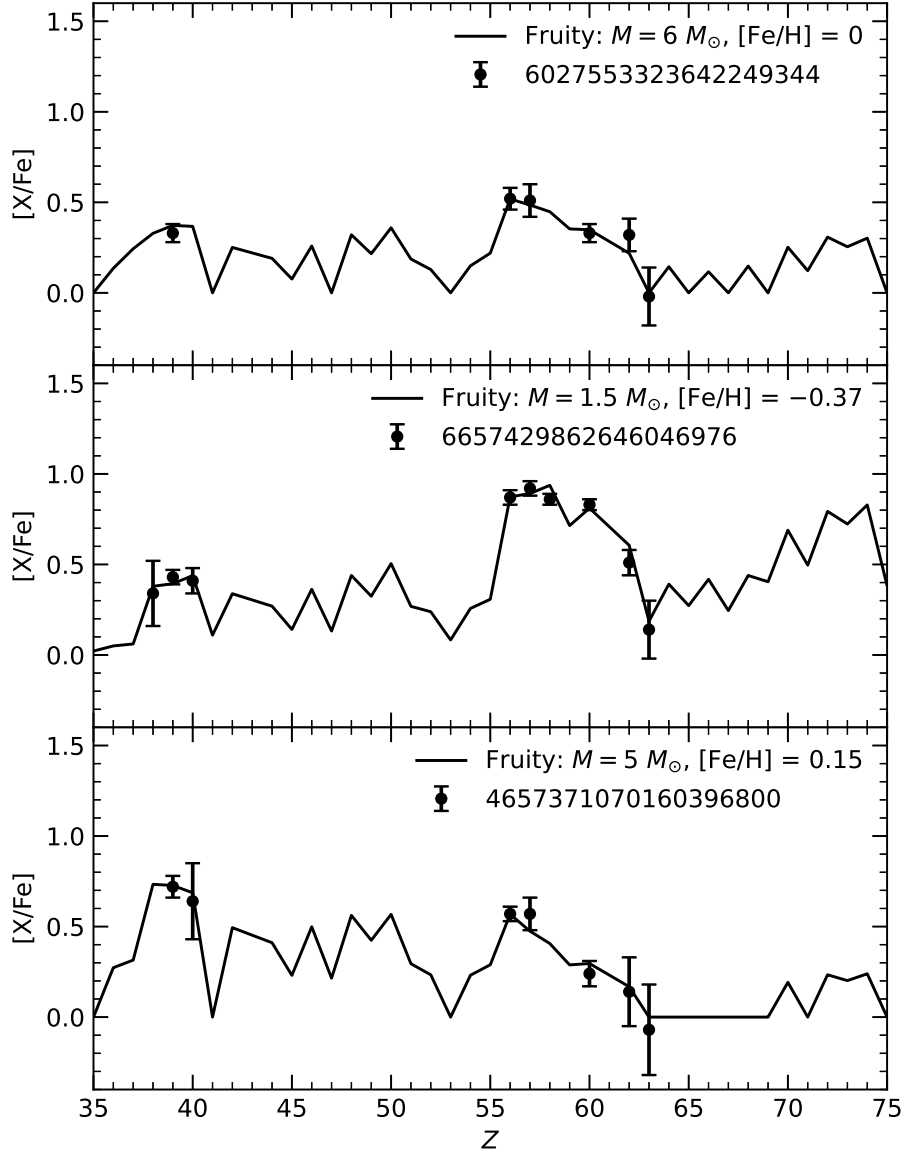


Figure 13. Comparison between the observed abundance patterns of the three sample stars (filled circles with error bars) and the best-fitting FRUITY AGB model predictions (curves) after applying dilution.

elements originate from nucleosynthetic sites distinct from those of the iron-peak elements. The sharp decrease in  $[i/Fe]$  ratios at low metallicities likely reflects the limited contribution of  $s$ -process nucleosynthesis in the early Galaxy. At comparable metallicities, the  $[i/Fe]$  ratios of Ba dwarfs tend to deviate from the locus defined by Ba giants. No statistically significant radial dependence of the  $s$ -process enrichment efficiency is found within the spatial extent of our sample. Furthermore, the observed decline in the  $[hs/ls]$  ratio with increasing metallicity suggests enhanced neutron-capture efficiency at lower metallicities. The greater dispersion of  $[hs/ls]$

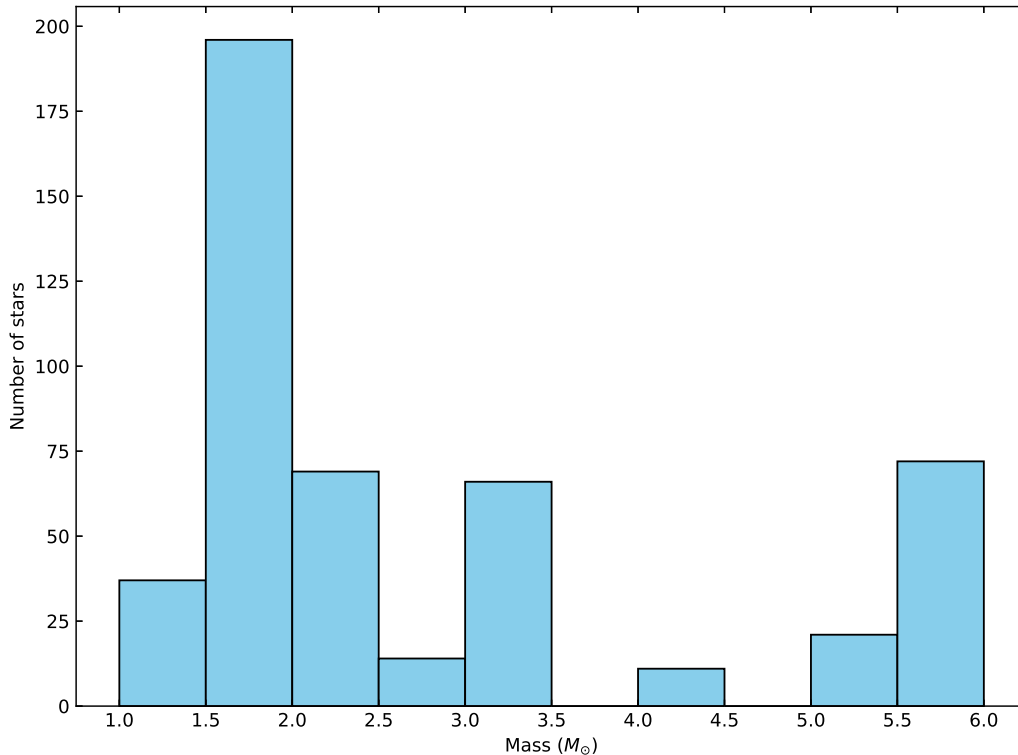


Figure 14. Histogram illustrating the mass distribution of companions to Ba stars.

at low  $[\text{Fe}/\text{H}]$  relative to high  $[\text{Fe}/\text{H}]$  likely reflects the progressive homogenization and mixing of the interstellar medium throughout Galactic evolution. No significant systematic differences are observed between the  $[\text{hs}/\text{ls}]$  distributions of Ba dwarfs and Ba giants. In addition, the  $[\text{C}/\text{Fe}]$  ratios of Ba giants show an overall decreasing trend with increasing  $[\text{Fe}/\text{H}]$ .

- Observations to date show that Ba stars include both giants and dwarfs, none of which are sufficiently evolved to synthesize  $s$ -process elements internally. Radial-velocity variations and NUV excesses revealed by SED analyses confirm their binary nature, indicating the presence of white-dwarf companions across the sample, with the exception of the Ba giant 6053735173729807872. For this star, no clear signatures of binarity are detected. If it is indeed part of a binary system, the lack of observable binary characteristics may be due to an orbital configuration unfavorable for detection or to a relatively cool companion incapable of producing a detectable NUV excess. Conversely, if the star is truly single, the origin of its  $s$ -process enhancements requires further investigation. The NUV excesses detected in the SEDs of Ba dwarfs are comparable to those observed in Ba giants, suggesting a similar underlying origin.
- For the 485 confirmed Ba binaries, companion masses inferred from FRUITY AGB models predominantly fall in the range of  $1.5\text{--}3.5 M_{\odot}$ , consistent with low-mass AGB stars that have undergone TDU episodes. Nevertheless, a number of Ba stars, comprising both dwarfs and giants, have inferred companion masses above  $5.0 M_{\odot}$ . This indicates that intermediate-mass stars undergoing the AGB phase and synthesizing  $s$ -process elements can also play a role in enriching Ba binaries. The dilution-corrected AGB model yields successfully reproduce the observed abundance patterns, providing strong support for the mass-transfer scenario for the formation of Ba stars.

We hope that this catalog will provide a valuable foundation for future studies of large Ba star samples, including binary-orbit monitoring and chemodynamical modeling. Expanding the sample size will be crucial for gaining deeper insights into  $s$ -process nucleosynthesis in AGB stars and the mass-transfer mechanisms operating in binary systems.

#### DATA AVAILABILITY

This paper made use of the publicly available GALAH DR4 (<https://www.galah-survey.org>), Gaia DR3 data (<https://www.cosmos.esa.int/gaia>), and StarHorse catalogs (Queiroz et al. 2023). The data underlying this paper are available in machine-readable form.

#### CODE AVAILABILITY

We use the standard data analysis tools as follows: TOPCAT (Taylor 2005), Matplotlib (Hunter 2007), NumPy (Harris et al. 2020), SciPy (Virtanen et al. 2020), Jupyter (Kluyver et al. 2016), Astropy (Astropy Collaboration et al. 2013, 2018, 2022), and Gala (Price-Whelan 2017).

1 We thank the referee for the constructive comments and suggestions, which have significantly improved the manuscript.  
 2 This work is supported by the National Natural Science Foundation of China (NSFC) under grant Nos. 12588202,  
 3 12273055, and 12503024; the National Key R&D Program of China under grant Nos. 2023YFE0107800 and  
 4 2024YFA1611902; the China Manned Space Program under grant No. CMS-CSST-2025-A13; the Ministry of Sci-  
 5 ence and Technology of China under grant No. 2023FY101104; the International Partnership Program of the Chi-  
 6 nese Academy of Sciences under grant No. 178GJHZ2022040GC; the Independent Research Program of the Na-  
 7 tional Astronomical Observatories, Chinese Academy of Sciences under grant No. E4ZB0301; the Strategic Priority  
 8 Research Program of the Chinese Academy of Sciences under grant No. XDB1160301; and the Fundamental Re-  
 9 search Funds of China West Normal University under grant No. 22ke041. We acknowledge the support from the  
 10 2 m Chinese Space Station Telescope project. This work made use of the Fourth Data Release of the GALAH  
 11 Survey (Bunder et al. 2024). The GALAH Survey is based on data acquired through the Australian Astronomi-  
 12 cal Observatory, under programs: A/2013B/13 (The GALAH pilot survey); A/2014A/25, A/2015A/19, A2017A/18  
 13 (The GALAH survey phase 1); A2018A/18 (Open clusters with HERMES); A2019A/1 (Hierarchical star forma-  
 14 tion in Ori OB1); A2019A/15, A/2020B/23, R/2022B/5, R/2023A/4, R2023B/5 (The GALAH survey phase 2);  
 15 A/2015B/19, A/2016A/22, A/2016B/10, A/2017B/16, A/2018B/15 (The HERMES-TESS program); A/2015A/3,  
 16 A/2015B/1, A/2015B/19, A/2016A/22, A/2016B/12, A/2017A/14, A/2020B/14 (The HERMES K2-follow-up pro-  
 17 gram); R/2022B/02 and A/2023A/09 (Combining asteroseismology and spectroscopy in K2); A/2023A/8 (Resolv-  
 18 ing the chemical fingerprints of Milky Way mergers); and A/2023B/4 (*s*-process variations in southern globular  
 19 clusters). We acknowledge the traditional owners of the land on which the AAT stands, the Gamilaraay people,  
 20 and pay our respects to elders past and present. This paper includes data that has been provided by AAO Data  
 21 Central ([datacentral.org.au](http://datacentral.org.au)). This work has made use of data from the European Space Agency (ESA) mission  
 22 Gaia (<https://www.cosmos.esa.int/gaia>), processed by the Gaia Data Processing and Analysis Consortium (DPAC,  
 23 <https://www.cosmos.esa.int/web/gaia/dpac/consortium>). Funding for the DPAC has been provided by national in-  
 24 stitutions, in particular the institutions participating in the Gaia Multilateral Agreement.

#### REFERENCES

- Abbott, B. P., Abbott, R., Abbott, T. D., et al. 2017, *ApJL*, 850, L39
- Allen, D. M., & Barbuy, B. 2006a, *A&A*, 454, 895
- Allen, D. M., & Barbuy, B. 2006b, *A&A*, 454, 917
- Arcones, A., & Thielemann, F. K. 2023, *A&ARv*, 31, 1A
- Asplund, M., Grevesse, N., Sauval, A. J., & Scott, P., 2009, *ARA&A*, 47, 481
- Astropy Collaboration, Robitaille, T. P., Tollerud, E. J., et al. 2013, *A&A*, 558, A33
- Astropy Collaboration, Price-Whelan, A. M., Sipócz, B. M., et al. 2018, *AJ*, 156, 123
- Astropy Collaboration, Price-Whelan, A. M., Lim, P. L., et al. 2022, *ApJ*, 935, 167
- Bayo, A., Rodrigo, C., & Barrado Y Navascués, D. 2008, *A&A*, 492, 277
- Beers, T. C., & Christlieb, N. 2005, *ARA&A*, 43, 531
- Belokurov, V., Erkal, D., Evans, N. W., et al. 2018, *MNRAS*, 478, 611
- Belokurov, V., Sanders, J. L., Fattahi, A., et al. 2020, *MNRAS*, 494, 3880
- Bennett, M., & Bovy, J. 2019, *MNRAS*, 482, 1417
- Bianchi, L., Shiao, B., & Thilker, D. 2017, *ApJS*, 230, 24
- Bidelman, W. P., & Keenan, P. C. 1951, *ApJ*, 114, 473
- Bisterzo, S., Gallino, R., Straniero, O., et al., 2012, *MNRAS*, 422, 849
- Böhm-Vitense, E., Carpenter, K., Robinson, R., et al. 2000, *ApJ*, 533, 969
- Brusadin, G., Matteucci, F., & Romano, D. 2013, *A&A*, 554, A135

- Bunder, S., Kos, J., Wang, E. X., et al. 2024, PASA, 42, e051
- Burbidge, E. M., Burbidge, G. R., Fowler, W. A., & Hoyle, F. 1957, RvMP, 29, 547
- Burris, D. L., Pilachowski, C. A., Armandroff, T. E., et al. 2000, ApJ, 544, 302
- Busso, M., Gallino, R., & Wasserburg, G. J. 1999, ARA&A, 37, 239
- Busso M., Gallino R., Lambert D. L., Travaglio T., Smith V. V. 2001, ApJ, 557, 802
- Carrillo, A., Deason, A. J., Fattahi, A., et al. 2024, MNRAS, 527, 2165
- Castelli, F., & Kurucz, R. L. 2004, IAUS, 210, A20
- Chen, Y. Q., Nissen, P. E., & Zhao, G. 2004, A&A, 425, 697
- Chen, T. Y., Shi, J. R., Yan, H. L. 2025, ApJ, 982, 182
- Cristallo, S., Piersanti, L., Straniero, O., et al. 2011, ApJS, 197, 17
- Cseh, B., Lugaro, M., D’Orazi, V., et al. 2018, A&A, 620, A146
- Cseh, B., Világos, B., Roriz, M. P., et al., 2022, A&A, 660, A128
- Cui, X. Q., Zhao, Y. H., Chu, Y. Q., et al. 2012, RAA, 12, 1197
- de Castro, D. B., Pereira, C. B., Roig, F., et al. 2016, MNRAS, 459, 4299
- De Silva, G. M., Freeman, K. C., Bland-Hawthorn, J., et al. 2015, MNRAS, 449, 2604
- Dodd, E., Callingham, T. M., Helmi, A., et al. 2023, A&A, 670, L2
- Escorza, A., Boffin, H. M. J., Jorissen, A., et al. 2017, A&A, 608, A100
- Escorza, A., Karinkuzhi, D., Jorissen, A., et al. 2019, A&A, 626, A128
- Escorza, A., Siess, L., Van Winckel, H., & Jorissen, A. 2020, A&A, 639, A24
- Gaia Collaboration, Recio-Blanco, A., Kordopatis, G., et al. 2023, A&A, 674, A38
- Gallino, R., Arlandini, C., Busso, M., et al. 1998, ApJ, 497, 388
- Gilmore, G., Wyse, R. F. G., & Norris, J. E. 2002, ApJ, 574, L39
- Gómez A. E., Luri X., Grenier S., et al. 1997, A&A, 319, 881
- Goriely, S. 1999, A&A, 342, 881
- Goswami, P. P., & Goswami, A. 2023, AJ, 165, 154
- Gray, R. O., & Corbally, C. J. 1994, AJ, 107, 742
- Han, Z. W., Eggleton, P. P., Podsiadlowski, P., & Tout, C. A. 1995, MNRAS, 277, 1443
- Han, J. J., Conroy, C., Johnson, B. D., et al. 2022, AJ, 164, 249
- Harris, C. R., Millman, K. J., van der Walt, S. J., et al. 2020, Nature, 585, 357
- Helmi, A., Babusiaux, C., Koppelman, H. H., et al. 2018, Nature, 563, 85
- Horta, D., Schiavon, R. P., Mackereth, J. T., et al. 2023, MNRAS, 520, 5671
- Hunter, J. D. 2007, CSE, 9, 90
- Johnson, D. R. H., & Soderblom, D. R. 1987, AJ, 93, 864
- Jorissen, A., Van Eck, S., Mayor, M., & Udry, S. 1998, A&A, 332, 877
- Jorissen A., Boffin H. M. J., Karinkuzhi D., et al. 2019, A&A, 626, A127
- Käppeler, F., Gallino, R., Bisterzo, S., & Aoki, W. 2011, RvMP, 83, 157
- Karinkuzhi, D., Van Eck, S., Jorissen, A., et al. 2018, A&A, 618, A32
- Karinkuzhi, D., Van Eck, S., Goriely, S., et al. 2021, A&A, 645, A61
- Karinkuzhi, D., Van Eck, S., Jorissen, A., et al. 2021, A&A, 654, A140
- Kluyver, T., Ragan-Kelley, B., Pérez, F., et al. 2016, in Loizides F., Schmidt B., eds
- Kong, X. M., Kumar, Y. B., Zhao, G., et al. 2018, MNRAS, 474, 2129
- Laporte, C. F. P., Gómez, F. A., Besla, G., et al. 2018, MNRAS, 473, 1218
- Lebzelter, T., Uttenthaler, S., Straniero, O., & Aringer, B. 2013, A&A, 554, A30
- Liang, Y. C., Zhao, G., & Zhang, B. 2000, A&A, 363, 555
- Liang, Y. C., Zhao, G., Chen, Y. Q., et al. 2003, A&A, 397, 257
- Liu, G. Q., Liang, Y. C., & Deng, L. C. 2009, RAA, 4, 431
- Liu, S., Wang, L., Shi J. R., et al. 2021, RAA, 21, 278
- Lu, P. K., Dawson, D. W., Uggren, A. R., & Weis, E. W. 1983, ApJS 52, 169
- Lu, P. K. 1991, AJ, 101, 2229
- Majewski, S. R., Schiavon, R. P., Frinchaboy, p. M., et al. 2017, AJ, 154, 94
- Matteucci, F. 2021, A&AR, 29, 5
- Mészáros, S., & Prieto, C. A. 2013, MNRAS, 430, 3285
- McClure, R. D., Fletcher, J. M., & Nemec, J. M. 1980, ApJ, 238, L35
- McClure, R. D., & Woodsworth, A. W. 1990, ApJ, 352, 709
- McMillan, P. J. 2017, MNRAS, 465, 76
- Naidu, R. P., Conroy, C., Bonaca, A., et al. 2020, ApJ, 901, 48
- Norfolk, B. J., Casey, A. R., Karakas, A. I., et al. 2019, MNRAS, 490, 2219
- Pereira, C. B., Sales Silva, J. V., Chavero, C., et al. 2011, A&A, 533, A51

- Pourbaix, D., Tokovinin, A. A., Batten, A. H., et al. 2004, *A&A*, 424, 727
- Price-Whelan, A. M. 2017, *JOSS*, 2, 388
- Purandardas, M., Goswami, A., Goswami, P. P., et al. 2019, *MNRAS*, 486, 3266
- Qian, Y. Z., & Wasserburg, G. J. 2007, *PhR*, 442, 237
- Queiroz, A. B. A., Anders, F., Chiappini, C., et al. 2023, *A&A*, 673, A155
- Rekhi, P., Sagi, B. A., Hallakoun, N., et al. 2024, *ApJL*, 973, L56
- Rojas, M., Drake, N. A., Pereira, C. B., et al. 2013, *Astrophysics*, 56, 57
- Roriz, M. P., Lugaro, M., Pereira, C. B., et al. 2021a, *MNRAS*, 501, 5834
- Roriz, M. P., Lugaro, M., Pereira, C. B., et al. 2021b, *MNRAS*, 507, 1956
- Roriz, M. P., Holanda, N., et al. 2024, *AJ*, 167, 184
- Roriz, M. P., Drake, N. A., Holanda, N., et al. 2025, *AJ*, 170, 259
- Ryu, T., Sari, R., de Mink, S. E., et al. 2025, *A&A*, 702, A61
- Schönrich, R., Binney, J., & Dehnen, W. 2010, *MNRAS*, 403, 1829
- Sheinis, A., Anguiano, B., Asplund, M., et al. 2015, *Journal of Astronomical Telescopes, Instruments, and Systems*, 1, 035002
- Shejeelammal, J., Goswami, A., Goswami, P. P., et al. 2020, *MNRAS*, 492, 3708
- Shetye, S., Van Eck, S., Goriely, S., et al. 2020, *A&A*, 635, L6
- Snedden, C., Cowan, J. J., & Gallino, R. 2008, *ARA&A*, 46, 241
- Stancliffe, R. J. 2021, *MNRAS*, 505, 5554
- Taylor, M. B. 2005, *ASPC*, 347, 29T
- Travaglio, C., Galli, D., Gallino, R., et al. 1999, *ApJ*, 521, 691
- Travaglio, C., Burkert, A., & Galli, D. 2001, *NuPhA. A*, 688, 396
- Travaglio, C., Gallino, R., Arnone, E., et al. 2004, *ApJ*, 601, 864
- Virtanen, P., Gommers, R., Oliphant, T. E., et al. 2020, *NatMe*, 17, 261
- Warner, B. 1965, *MNRAS*, 129, 263
- Williams, P. M. 1975, *MNRAS*, 170, 343
- Yang, G. C., Liang, Y. C., Spite, M., et al. 2016, *RAA*, 16, 19
- Yang, G. C., Zhao, J. K., Liang, Y. C., et al. 2024, *MNRAS*, 534, 3104
- Yong, D., Norris, J. E., Bessell, M. S., et al. 2013, *ApJ*, 762, 26
- Začs, L. 1994, *A&A*, 283, 937
- Zhao, G., Zhao, Y.H., Chu, Y. Q., et al. 2012, *RAA*, 12, 723